SAND2009-4124C

Dislocations in $LaBr_3$ crystals

X. W. Zhou[1,*], F. P. Doty[2], and Pin Yang[3]

[1] *Mechanics of Materials Department, Sandia National Laboratories, Livermore, California 94550, USA*

[2] *Engineered Materials Department, Sandia National Laboratories, Livermore, California 94550, USA*

[3] *Ceramic and Glass Department, Sandia National Laboratories, Albuquerque, NM 87185, USA*

ABSTRACT

Using a many-body embedded ion method potential for La-Br system, molecular dynamics simulations have been performed to study dislocations in the UCl_3 type of $LaBr_3$ crystal including identification of dislocation line energy, core structure, migration mechanism, and mobility. We found that dislocations with the $<0001>$ Burgers vector can move under shear stresses, but they retain perfect dislocations during the motion rather than dissociated partials as commonly seen in metal systems. Unlike the $<0001>$ edge dislocations whose mobility increases with temperature, the $<0001>$ screw dislocations may become sessile at high temperatures due to thermally activated dissociation of the core. Dislocations with the $<11\bar{2}0>$ Burgers vector were found to be sessile due to non-planar dissociation at the core. Because the $<0001>$ dislocations can only slip on the $\{1\bar{1}00\}$ prism plane and often only the edge dislocations are operative, the stresses created during any thermal mechanical processes cannot be effectively relieved by the plastic deformation mechanism. Considering that $LaBr_3$ tend to cleave along the $\{1\bar{1}00\}$ prism plane, the simulations shed some lights on why this material is so brittle and how large $LaBr_3$ crystals tend to fracture during growth.

Keywords: $LaBr_3$, molecular dynamics, dislocation, mechanical property, interatomic potential, slip systems, scintillator

1. INTRODUCTION

$LaBr_3$ crystal has superior scintillating properties, and is being widely explored for gamma ray spectroscopy applications[1,2]. A large volume, high quality $LaBr_3$ single crystal is the key for this application as it enables a maximum interaction between the material and the radiation. The yield of large volume crystals that can be grown today, however, is extremely low. The limiting problem is that the crystal would fracture along the $\{1\bar{1}00\}$ cleavage plane when the volume is grown above a threshold[3]. An improved synthesis of $LaBr_3$ crystals, therefore, relies on the understanding of the mechanical properties of this complicated, ionically-bonded crystal, and the development of methods that can mitigate the fracture during its growth. The study of mechanical properties of $LaBr_3$ crystals has been a prolonged process. This is because experimental methods that are effective in revealing deformation, fracture, and microstructure of materials cannot be easily applied to reveal atomic mechanisms specific to the $LaBr_3$ crystals. As a result, these mechanisms have not been well studied. Recently, a La-Br interatomic potential suitable for the crystal of the$LaBr_3$ compound has been developed[4]. This enables large scale molecular dynamics (MD) simulations to be used to study precisely the atomic mechanisms of the mechanical processes of the

* Corresponding author. Tel.: 1 925 294 2851; fax: 1 925 294 3410. E-mail address: xzhou@sandia.gov (X. W. Zhou)

material. Here we report our MD study on the dislocations in single crystalline $LaBr_3$ solid compound. Dislocation line energy, core structure, migration mechanism, and mobility are all quantified.

2. INTERATOMIC POTENTIAL

Compared with metal and semiconductor materials, the ionic La-Br system has been far less explored and therefore there are only few interatomic potential currently available for this system[4,5]. On the other hand, the solid compound $LaBr_3$ exhibits an equilibrium $P6_3/m$ (UCl_3) crystal structure[6,7,8]. This phase is relatively complicated to model as it has a hexagonal lattice with a small lattice constant ratio of c/a ≈ 0.57, a local rotation of Br polyhedron surrounding each La atom, a slightly longer bond length between La and the cap Br atoms than that between La and the prism Br atoms, the presence of big lattice hollows, and the cleavage fracture along the $\{1\bar{1}00\}$ plane[6,7]. The many-body embedded ion method (EIM) potential we developed earlier has been demonstrated to be able to capture all these features in addition to a correct description of lattice constants and cohesive energies of various phases[4,8,9,10]. As a result, the EIM potential was used in the present work.

3. DISLOCATION ENERGY CALCULATIONS

Dislocation line energies were first calculated. Various Burgers vectors were considered and they were narrowed down to $<0001>$ and $<11\bar{2}0>$ as the magnitudes (and therefore the dislocation energies) of other vectors significantly larger. The $<0001>$ Burgers vector can slip on the $\{1\bar{1}00\}$ prism plane. The $<11\bar{2}0>$ Burgers vector can slip on both the prism and the $\{0001\}$ basal plane. Here we calculated energies of both edge and screw dislocations with both $<0001>$ and $<11\bar{2}0>$ Burgers vectors, considering both the basal and the prism slip planes for the $<11\bar{2}0>$ Burgers vector.

Of the hexagonal $LaBr_3$ crystal, an orthogonal cell can be chosen with a in the $<11\bar{2}0>$ direction, $2a\cdot\cos(\pi/6)$ in the $<1\bar{1}00>$ direction, and c in the $<0001>$ direction, where a and c are lattice constants of the hexagonal cell. We therefore used rectangular computational crystals with the dislocation lying in the z direction. Periodic boundary conditions were used in the x and z directions and free boundary conditions were used in the y direction. This geometry corresponds to an array of infinitely long dislocations stacked in the x direction. The crystal dimensions and orientations used to model different types of dislocations are listed in Table I. The x-y dimension was chosen to be around ~ 480×250 $Å^2$, which was found to be sufficiently large so that the effect of interaction between dislocation and system boundary can be neglected.

Table I. Orientation and dimension of crystals for dislocation energy calculations.

Dislocation	Crystal orientation			Dimension (cells/Å)		
	x	y	z	x	y	z
$\langle 0001\rangle$ edge	$\langle 0001\rangle$	$\langle\bar{1}100\rangle$	$\langle 11\bar{2}0\rangle$	104/470.7	18/247.9	8/63.6
$\langle 0001\rangle$ screw	$\langle 11\bar{2}0\rangle$	$\langle\bar{1}100\rangle$	$\langle 0001\rangle$	60/477.1	18/247.9	4/18.1
$\langle 11\bar{2}0\rangle$ edge, basal slip	$\langle 11\bar{2}0\rangle$	$\langle 0001\rangle$	$\langle\bar{1}100\rangle$	60/477.1	54/244.4	4/55.1
$\langle 11\bar{2}0\rangle$ screw, basal slip	$\langle\bar{1}100\rangle$	$\langle 0001\rangle$	$\langle 11\bar{2}0\rangle$	34/468.3	54/244.4	2/15.9
$\langle 11\bar{2}0\rangle$ edge, prism slip	$\langle 11\bar{2}0\rangle$	$\langle\bar{1}100\rangle$	$\langle 0001\rangle$	60/477.1	18/247.9	14/63.4
$\langle 11\bar{2}0\rangle$ screw, prism slip	$\langle 0001\rangle$	$\langle\bar{1}100\rangle$	$\langle 11\bar{2}0\rangle$	104/470.7	18/247.9	2/15.9

In an atomistic simulation, the dislocation line energy Γ can be accurately calculated as:

$$\Gamma = \frac{E_{dis} - E_{perf}}{L}, \tag{1}$$

where E_{dis} and E_{perf} are the total energies of the atomistic system with and without the dislocation, and L is the total length of the dislocation. Perfect crystals can be created by assigning coordinates to atoms based upon the lattice sites. The following specific atomistic models were used in the present work to introduce edge and screw dislocations.

2.1 Edge dislocation model

The underlying assumption behind Eq. (1) is that the perfect and the dislocated crystals have the same number of atoms and the same geometry. However, edge dislocations are associated with missing or extra half planes. Unlike the past atomistic dislocation models that create missing or extra half planes[11,12,13], our approach to create the edge dislocation does not change the number of atoms. The model is illustrated in Fig. 1, where a perfect crystal prior to the dislocation creation is shown. This crystal is divided into several regions. The blue regions at the left and the right sides are the boundary regions that remain fixed during dislocation creation. The upper blue and lower red regions in the middle of the system are initially misaligned by a Burgers vector of the dislocation. The middle blue region is then displaced to the left by half of the Burgers vector whereas the middle red region is displaced to the right by another half of the Burgers vector so that the two regions become aligned after the displacement. All other atoms between the middle and the side boundary regions are ramped according to a linear elastic deformation. This operation is equivalent to inserting upper half planes in the left half of the system and lower half planes in the right half of the system, thereby creating two edge dislocations of opposite sign along the z direction. Note that the middle blue and red regions are shifted with respect to each other by a perfect lattice vector, and therefore no defects are created within the boundary regions.

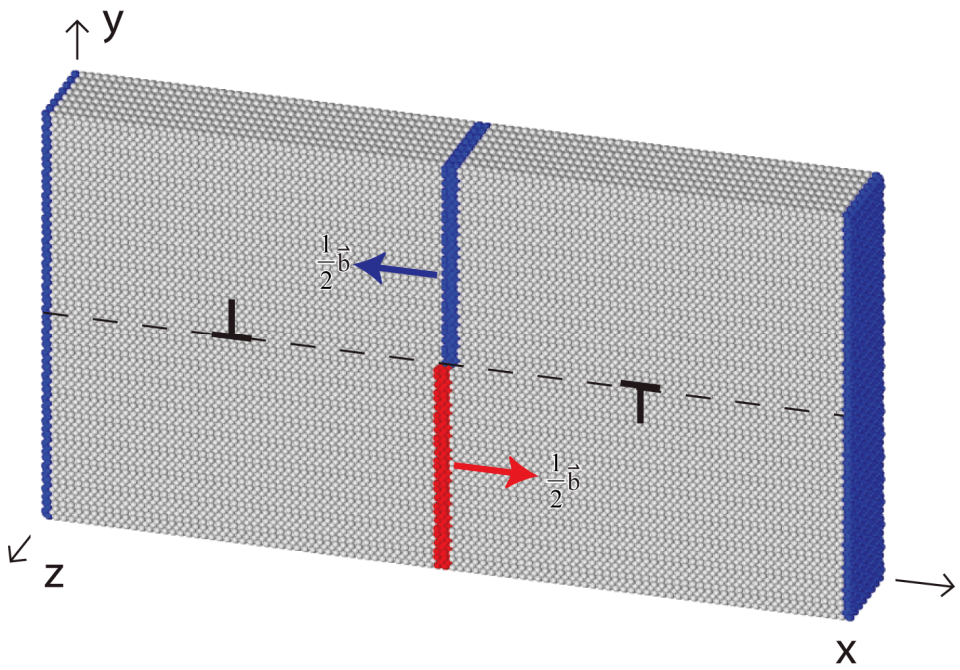

Fig. 1. Edge dislocation model for energy calculation.

2.2 Screw dislocation model

The screw dislocation model is illustrated in Fig. 2. As in the edge dislocation case, the blue atoms at the left and the right sides are the boundary atoms that remain fixed during dislocation creation. Unlike the edge dislocation model, the upper blue and lower red regions in the middle of the system are initially aligned. During creation of dislocations, the middle blue region is displaced in the negative z direction by half of the Burgers vector whereas the middle red region is displaced in the positive z direction by another

half of the Burgers vector so that the two regions remain perfect lattice after the displacement. The displacements of all other atoms between the middle and the side boundary regions are ramped based on the spiral angle, the atom distance from the dislocation core, and any boundary constrains that may exist[14]. This operation creates two screw dislocations of opposite sign along the z direction, Fig. 3(b), where the x-y coordinates of the two dislocation cores were taken respectively as the geometry centers of the left and the right halves of the system.

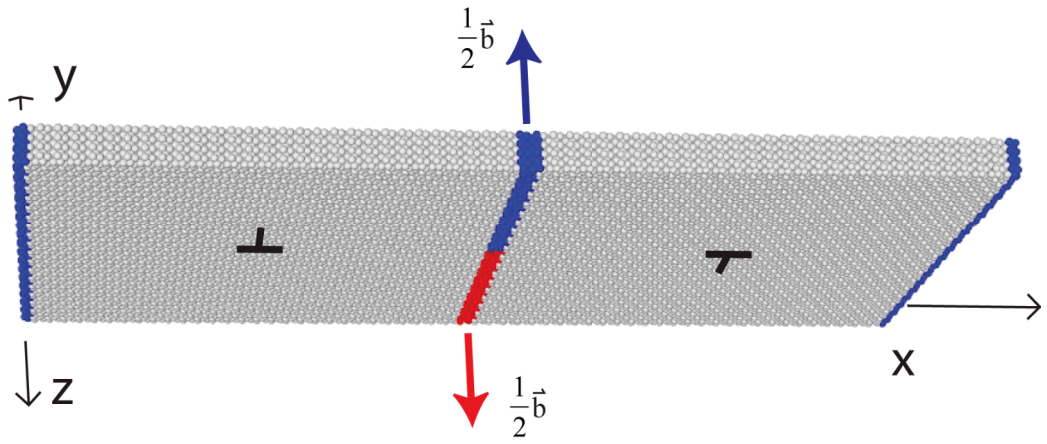

Fig. 2. Screw dislocation model for energy calculation.

2.3 Energy calculations

Molecular statics energy minimization simulations were performed to calculate the total relaxed energies of both perfect and dislocated crystals under the constraint of fixed positions for all atoms in the blue and red regions. As the width of the middle and side boundary regions was chosen to be larger than the cutoff distance of the interatomic potential, atoms at the left half of the system did not see those at the right half. As a result, there was no interaction between the two dislocations. The total system energies were used in Eq. (1) to calculate dislocation line energies Γ. The results are shown in Table II.

Table II. Dislocation line energies Γ.

Burgers vector	$\langle 0001 \rangle$		Basal $\langle 11\bar{2}0 \rangle$		Prism $\langle 11\bar{2}0 \rangle$	
Dislocation type	edge	screw	edge	screw	edge	screw
Γ (eV/Å)	4.7	5.8	10.8	8.2	12.1	12.0

Table II indicates that the energy of $<11\bar{2}0>$ dislocations is significantly higher than that of $<0001>$ dislocations. We can see that the magnitudes of the Burgers vectors of the $<0001>$ and the $<11\bar{2}0>$ dislocations are respectively $b_1 = 4.526$ Å and $b_2 = 7.951$ Å. As a result, $(b_2/b_1)^2 = 3.1$. The significantly higher energy for the $<11\bar{2}0>$ dislocation is therefore consistent with its significantly higher value of $(b_2)^2$. Interestingly, Table II also shows that the $<0001>$ screw dislocation has a higher energy than the $<0001>$ edge dislocation. We found that if the energy of the system is not relaxed, then $<0001>$ edge dislocation would have significantly higher energy than the $<0001>$ screw dislocation. As a result, the higher screw dislocation energy is a result of the relaxed dislocation core structures. Table II clearly indicates that the lowest energy $<0001>$ dislocations dominate the mechanical properties of the $LaBr_3$ crystals.

4. DISLOCATION MOBILITY CALCULATIONS

Molecular dynamics simulations were performed to study dislocation mobility and its dynamics under a shear stress. The focus of this study is to understand the possible slip on prism and basal planes. The $<0001>$ and the $<11\bar{2}0>$ dislocations can both slip on the $\{1\bar{1}00\}$ prism plane. However, the $<0001>$ dislocation has significantly lower energy and hence is expected to dominate the prism slip. As a

result, only the <0001> dislocation was studied for the prism slip. The basal $<11\bar{2}0>$ dislocation was studied for the basal slip as it is the only dislocation available for that slip.

The crystal orientation and dimension used for the study are shown in Table III. Periodic boundary conditions were used in the x and z directions and free boundary conditions were used in the y direction. It should be noted that dislocation models shown in Figs. 1 and 2 cannot be used for dislocation dynamics simulations because the two opposite dislocations would cancel once they are allowed to move. The following alternative dislocation models were therefore used.

Table III. Orientation and dimension of crystals for dislocation dynamics simulations.

Dislocation	Crystal orientation			Dimension (cells/Å)		
	x	y	z	x	y	z
$\langle 0001 \rangle$ edge	$\langle 0001 \rangle$	$\langle 1\bar{1}00 \rangle$	$\langle 11\bar{2}0 \rangle$	50/226.3	6/82.6	2/15.9
$\langle 0001 \rangle$ screw	$\langle 11\bar{2}0 \rangle$	$\langle 1\bar{1}00 \rangle$	$\langle 0001 \rangle$	60/477.1	18/247.9	4/18.1
Basal $\langle 11\bar{2}0 \rangle$ edge	$\langle 11\bar{2}0 \rangle$	$\langle 0001 \rangle$	$\langle 1\bar{1}00 \rangle$	30/238.5	20/90.5	2/27.5
Basal $\langle 11\bar{2}0 \rangle$ screw	$\langle 1\bar{1}00 \rangle$	$\langle 0001 \rangle$	$\langle 11\bar{2}0 \rangle$	34/468.3	54/244.4	3/23.9

4.1 Edge dislocation model

The edge dislocation model for dynamics simulation is demonstrated in Fig. 3. Several steps are involved to create the dislocation. First, several atomic planes of atoms are removed from the upper half of the crystal. The width of the removed planes corresponds to the magnitude of the Burgers vector b. To close the gap, atoms at the left edge of the gap are displaced to the right by b/2, and atoms at the right edge of the gap are displaced to the left by another b/2, with the positions of all other atoms in the upper half of the system ramped linearly. Finally, the system is strained in the x direction by an appropriate strain so that the system dimension in the x direction is approximately the average of the lattice sizes of the upper and lower crystals. By using periodic boundary condition in the x direction, such a dislocation model essentially creates an array of edge dislocations that are equally spaced by the periodic length in the x direction.

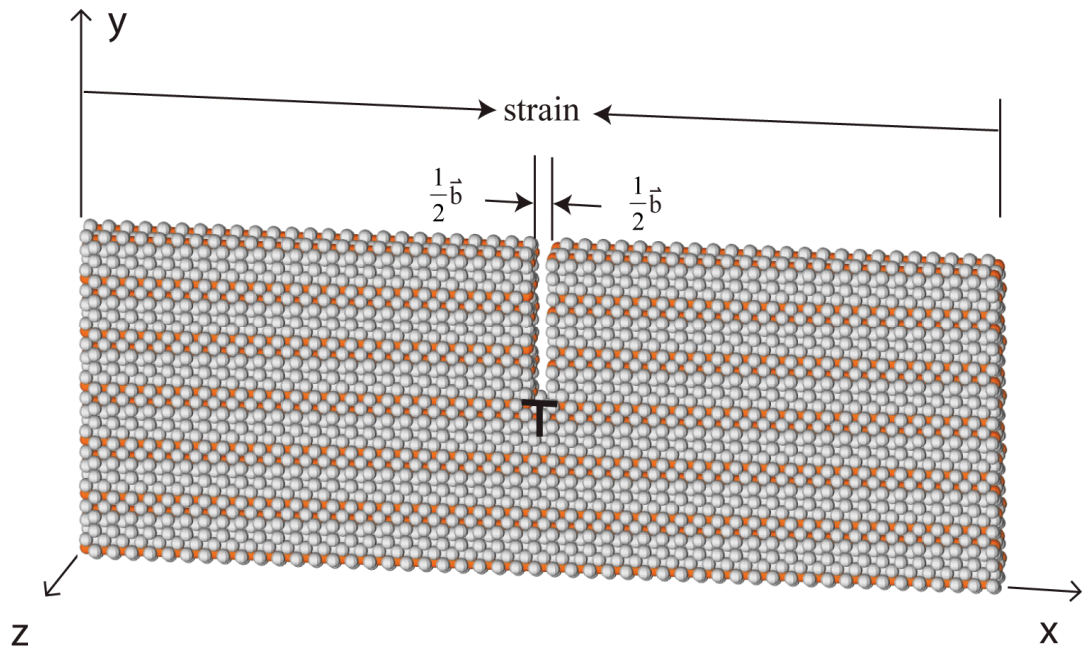

Fig. 3. Edge dislocation model for mobility simulation.

4.2 Screw dislocation model

The screw dislocation model for dynamics simulation is shown in Fig. 4. First, the upper right half of the crystal is displaced by b/2 in the negative z direction and the lower right half of the crystal is displaced by b/2 in the positive z direction. Corresponding ramping displacements are made to atoms in the left half of the crystal based on the spiral angle, their distance from the dislocation core (the geometry center of the left half of the system), and the boundary constraints. This creates a screw dislocation in the left half of the system, and the right half of the system remains perfect because the relative displacement between the upper and lower halves is a perfect lattice vector $\vec{b}$. This process, however, destroys the periodic boundary condition in the x direction because the right boundary is shifted with respect to the left boundary by a partial lattice vector $\vec{b}$/2. To overcome this problem, a similar process is used to create a second screw dislocation in the right half of the system by displacing the upper right end of the system by b/2 in the negative z direction and the lower right end of the system by b/2 in the positive z direction while making corresponding ramping displacements to other atoms. This operation causes a total displacement of the right boundary with respect to the left boundary to be a lattice vector b, which enables the use of periodic boundary conditions. Under the periodic boundary conditions, this dislocation model allows us to simulate an array of screw dislocations. A minor difference from the edge dislocation model is that the computational cell now includes two independent dislocations. This means that the spacing between adjacent dislocations may dynamically change. The spacing between each pair of dislocations, however, is still fixed at the periodic length in the x direction just as the spacing between the adjacent dislocations in the edge dislocation model. Because we have chosen the x dimension of the screw dislocation model to be roughly double of that of the edge dislocation model, Table III, the average dislocation spacing is about the same for both models.

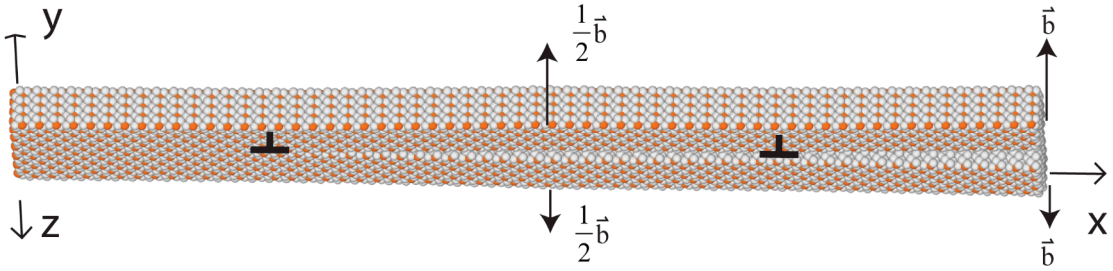

Fig. 4. Screw dislocation model for mobility calculation.

4.3 Loading and dislocation identification

Evolution of an edge dislocation under a shear stress τ_{yx} and a screw dislocation under a shear stress τ_{yz} was simulated using the MD method. The stress was maintained during an MD simulation by applying corresponding forces to a thin (5 to 10 Å thick) layer of surface atoms. Assume that the numbers of atoms per unit surface area are ζ_t and ζ_b respectively for the top and bottom surface layers, a shear stress $\tau_{y\alpha}$ (α = x or z) was created by applying constant forces $f_t = \tau_{y\alpha}/\zeta_t$ in the negative α direction to atoms in the top surface layer, and $f_b = \tau_{y\alpha}/\zeta_b$ in the positive α direction to atoms in the bottom surface layer. Note that for screw dislocation, $\zeta_t = \zeta_b$, and hence, $f_t = f_b$. For edge dislocation, $\zeta_t \neq \zeta_b$ due to missing half planes. As a result, $f_t \neq f_b$.

Initial crystals were created using the lattice constants equilibrated at a temperature of 0 K. MD simulations were performed using LAMMPS[15] at a time step size of 0.5 fs. An "nve" integrator[15] was applied to all atoms. A constant temperature simulation was achieved by rescaling velocities of all atoms that are not in the surface layers at each time step. For the target temperature of 0 K, the rescaling was performed only when the temperature rose above a 0.00001 K window to allow motion of atoms.

Dislocations can be identified using the slip vector developed previously[16]. The slip vector is defined as $\vec{S}_i = -\frac{1}{N_s}\sum_{j=1}^{N_j}\left(\vec{R}_{i,j} - \vec{R}^0_{i,j}\right)$, where $j = 1, 2, \ldots, N_j$ is a list of all neighbors to atom i, $\vec{R}^0_{i,j}$ is the vector from

atom *i* to a neighbor *j* in an initial perfect lattice configuration, $\vec{R}_{i,j}$ is the vector from atom *i* to the same neighbor *j* in the current configuration, and N_s is the number of neighbors that are on an adjacent slip plane to atom *i* (e.g., $N_s = 3$ if slip occurs on an {111} fcc lattice). By finding the relative displacement of a neighbor atom *j* with respect to a given atom *i*, it can be determined if a plane neighboring atom *i* has slipped and in what direction. Dividing by N_s scales the vector's magnitude so that it is equal to the magnitude of the Burgers vector of the slipping dislocation. This definition gives large magnitudes of slip vectors for all slipped atoms including those at the dislocation core and those trailing the dislocation. To isolate the dislocation core, we slightly modified the slip vector. First, the neighbor vector list $\vec{R}_{i,j}^{0,\alpha}$ from atom *i* to its neighbor *j* ($j = 1, 2, \ldots, N_j$) was determined from an initial perfect crystal for all atom *i* ($i = 1, 2, \ldots, N$). Note that we use the notation $\vec{R}_{i,j}^{0,\alpha}$ ($\alpha = 1, 2, \ldots$) here rather than $\vec{R}_{i,j}^{0}$. This is because (i) in the UCl_3 $LaBr_3$ structure, there are two non-equivalent Br sites (i.e., $\alpha = 2$), each with a different set of neighbor vector list; and (ii) we discovered that the migration of a screw dislocation causes the Br atoms to switch between these two different sites. Hence, it is necessary to track all possible local perfect lattices in order to determine if a Br atom has switched sites. Next, the neighbor vector list $\vec{R}_{i,k}$ ($k = 1, 2, \ldots, N_k$) for the current configuration was redetermined, where *k* does not necessarily correspond to *j* and N_j does not necessarily equal N_k. A *j* to *k* match was then performed by minimizing the difference between $\vec{R}_{i,j}^{0,\alpha}$ and $\vec{R}_{i,k}$. This results in a unique value of $\alpha = \alpha_0$ and a matched *j* as a function of *k*, *j*(*k*). The slip vector was finally calculated as $\vec{S}_i = -\frac{1}{N_s}\sum_{k=1}^{\min(N_j,N_k)}\left(\vec{R}_{i,k} - \vec{R}_{i,j(k)}^{0,\alpha_0}\right)$. Because $\vec{R}_{i,j}^{0,\alpha_0}$ is always referred to the current perfect lattice, the magnitude of the slip vector diminishes when dislocation completely sweeps through to recover a perfect crystal. As a result, the modified slip vector only shows the dislocation core. If no other defects form, then the maximum magnitude of the slip vector is close to half of the magnitude of the Burgers vector due to the round off of the current configuration with respect to the next closest perfect configuration.

4.4 Atomic configurations of dislocations

The time evolution of the <0001> edge dislocation at a temperature T of 0 K and a shear stress τ_{yx} of 2.0 GPa is shown in Fig. 5 by superimposing configurations obtained at different times. In Fig. 5, the shaded region represents the size of the simulated system projected onto the x-y plane, and atoms are shown using the color scheme based on the magnitude of the modified slip vector. For clarity, only atoms with magnitude of slip vector larger than 0.2 are displayed whereas all other atoms are invisible. Fig. 6 indicates that the modified slip vector provides a sharp contrast of the dislocation core. It can be seen that the <0001> edge dislocation moved rapidly under the applied shear stress of 2.0 GPa and the 0 K temperature. No dislocation dissociation into partials was observed and dislocation was seen to move in a perfect unit. The time evolution of the <0001> screw dislocation at 0 K and a shear stress τ_{yz} of 2.0 GPa is shown similarly in Fig. 6. Again a rapid dislocation motion is observed. Analysis also indicated that the screw dislocation migrated as a perfect unit dislocation.

Dislocation dynamics simulations were also performed for the <0001> dislocations at a higher temperature of 300 K. We discovered that the mobility of the edge dislocation was increased as the temperature was increased. Surprisingly, the screw dislocation became sessile at 300 K. On the other hand, simulations carried out for the basal $<11\bar{2}0>$ edge and screw dislocations indicated that these basal dislocations are also sessile. Furthermore, we discovered that when dislocations are in their sessile configurations, they dissociate into three-dimensional (3D) defects at the core. Clearly, this non-planar dissociation creates significant resistance to dislocation motion, resulting in sessile properties. For the <0001> screw dislocation, this 3D dissociated core structure has a slightly higher energy. However, it can be realized at a finite temperature through the thermally activated processes. As a result, the screw dislocation was seen to be mobile at 0 K but became sessile at 300 K. It is pointed out that the <0001>

screw dislocation intersects with three slip planes. This is similar to the screw dislocation in body-centered-cubic crystals, which also intersects with three slip planes, and is also non-planar and sessile[17].

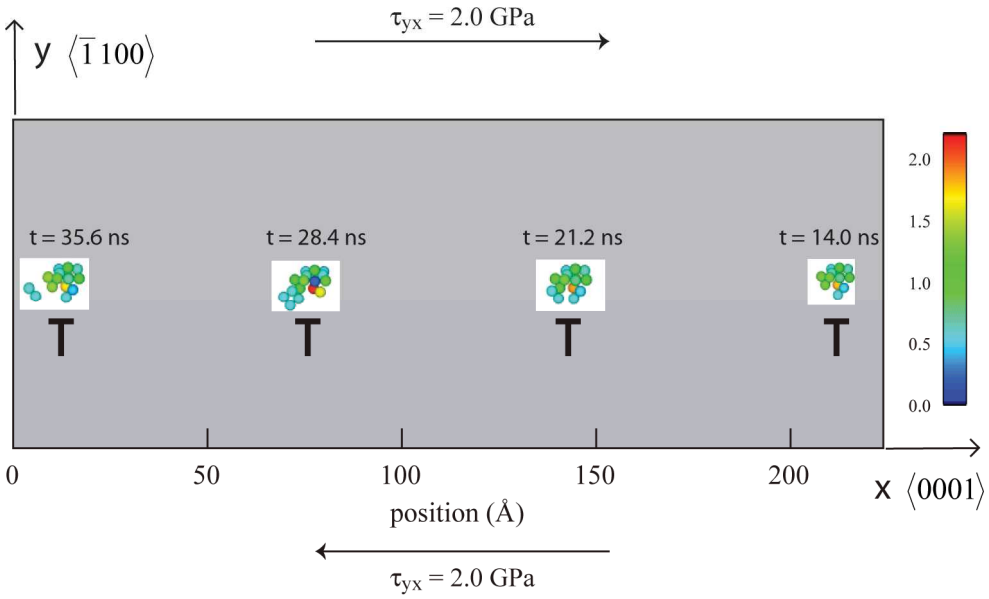

Fig. 5. Motion of < 0001 > edge dislocation at τ_{yx} = 2.0 GPa and T = 0 K.

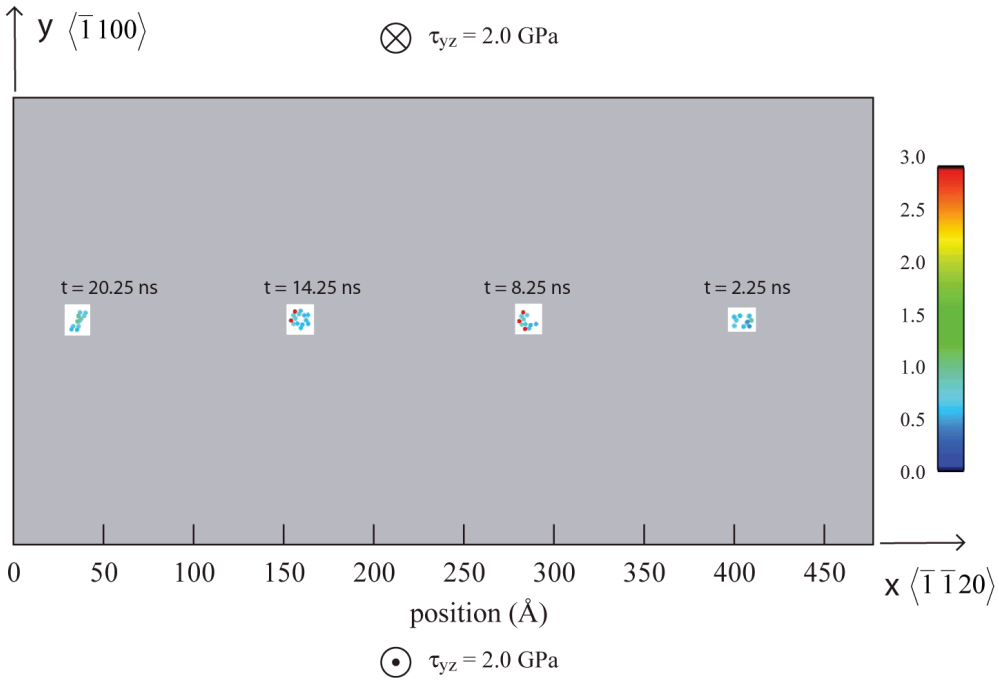

Fig. 6. Motion of < 0001 > screw dislocation at τ_{yx} = 2.0 GPa and T = 0K.

4.5 Critical flow stress for dislocation motion

The modified slip vector can be used to precisely identify the position of dislocation. Dislocation position was calculated as a function of time at different shear stresses and temperatures. The results

obtained at 0 K are shown in Figs. 7(a) and 7(b) respectively for the < 0001 > edge and screw dislocations. It can be seen that once the steady-state is reached, the dislocation location is a linear function of time. Clearly, dislocation dynamics exhibits a constant steady-state velocity. This velocity is seen to increase with the applied shear stress.

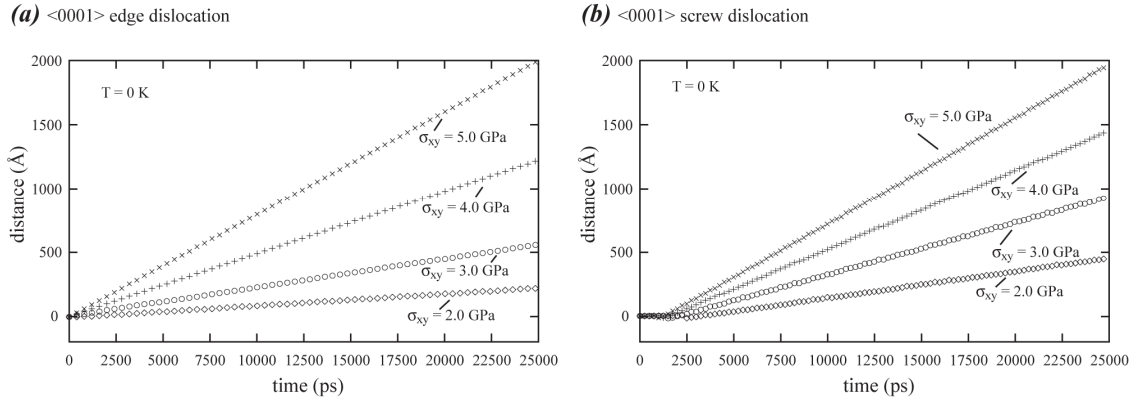

Fig. 7. $\langle 0001 \rangle$ dislocation position as a function of time at a stress of 2.0 GPa and a temperature of 0 K.

The steady-state velocities obtained at various shear stresses can be used to estimate a critical flow stress for the onset of dislocation motion. For better illustration purposes, we scaled the steady-state velocities by the velocity obtained at the maximum simulated stress. This relative steady-state velocity is plotted in Fig. 8 as a function of shear stress for the < 0001 > edge dislocation at both 0 and 300 K and the < 0001 > screw dislocation at 0 K. Fig. 8 indicates that the critical shear stress for both edge and screw dislocations at 0 K are near 1.5 GPa. Increasing the temperature to 300 K resulted in a reduced critical flow stress of 1.0 GPa for the < 0001 > edge dislocation. This reduction is expected because dislocations can move through thermally-activated processes. However, it should be noted that the MD simulations do not include all the possible thermally-activated mechanisms that may require time scales beyond the MD simulations. Consequently, the critical stress is likely to be overestimated. An additional finding from Fig. 8 is that at the highest simulated stress of 5.0 GPa, the steady-state velocity approached saturation at 300 K for the < 0001 > edge dislocations, but was far from saturation for both edge and screw dislocations at 0 K.

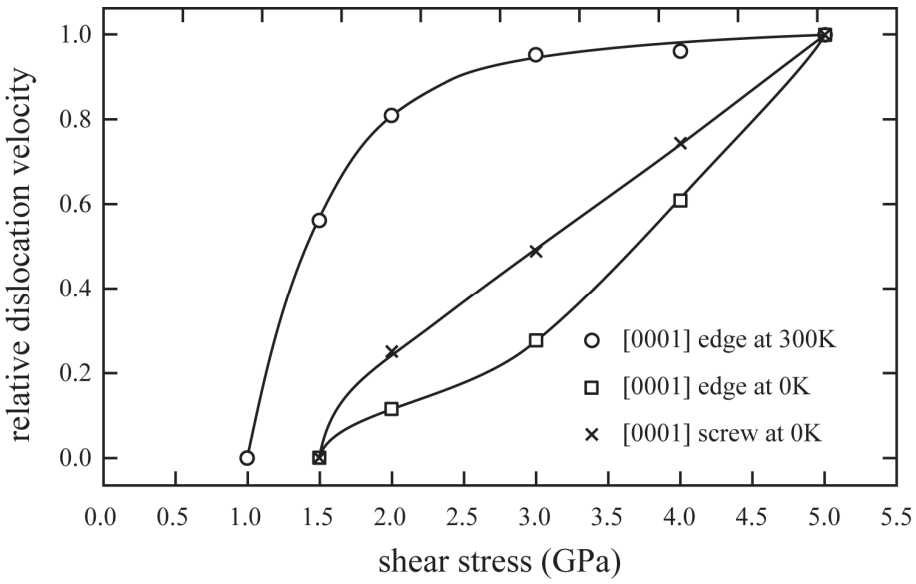

Fig. 8. Steady-state dislocation velocity as a function of stress.

5. CONCLUSIONS

Molecular dynamics simulations have been carried out to study dislocations of the UCl_3 type of $LaBr_3$ crystal. The following conclusions have been achieved:

1. Dislocation with the $<0001>$ Burgers vector has significantly lower energy than that with the $<11\bar{2}0>$ Burgers vector. For the $<0001>$ Burgers vector, the edge dislocation has slightly lower energy than the screw dislocation.
2. The $<0001>$ dislocation is mobile while the $<11\bar{2}0>$ dislocation is sessile. Because the $<0001>$ dislocation can only slip on the prism planes, no slip systems are available on the basal plane for $LaBr_3$.
3. The $<0001>$ dislocations in $LaBr_3$ do not dissociate into partials and they move in a perfect unit.
4. The mobility of the $<0001>$ edge dislocation increases with temperature. Contrarily, the $<0001>$ screw dislocation is mobile at 0 K but becomes sessile at 300 K. When in sessile configurations, all dislocations exhibit non-planar core structures.
5. The critical flow stress for the onset of motion of the $<0001>$ dislocations is 1.0 GPa for the edge dislocation at 300 K and 1.5 GPa for both edge and screw dislocations at 0 K.

6. ACKNOWLEDGEMENTS

Sandia is a multi-program laboratory operated by Sandia Corporation, a Lockheed Martin Company, for the United States Department of Energy's National Nuclear Security Administration under contract DEAC04-94AL85000. This project was sponsored by the US Department of Energy, NA22 Advanced Materials.

References

1 W. W. Moses, *Nucl. Ins. Meth. A*, **487**, 123 (2002).
2 A. Peurrung, *Mater. Today*, **11**, 50 (2008).
3 W. M. Higgins, A. Churilov, E. van Loef, J. Glodo, M. Squillante, and K. Shah, *J. Cryst. Growth*, **310**, 2085 (2008).
4 X. W. Zhou, and F. P. Doty, *Phys. Rev. B*, **78**, 224307(2008).
5 F. Hutchinson, M. Wilson, and P. A. Madden, *J. Phys: Condens. Matter*, **12**, 10389 (2000).
6 K. Kramer, T. Schleid, M. Schulze, W. Urland, and G. Meyer, *Z. Anorg. Allg. Chem.*, **575**, 61 (1989).
7 W. H. Zachariasen, *Acta Cryst.*, **1**, 265 (1948).
8 J. D. H. Donnay, and H. M. Ondik, *"crystal data, determinative tables"*, 3rd ed., Vol. 2 (inorganic compounds), U. S. Department of Commerce, National Bureau of Standards, and Joint Committee on Power Diffraction Standards, U. S. A., 1973.
9 D. Zamir, and D. S. Schreiber, *Phys. Rev. A*, **136**, 1087(1964).
10 I. Barin, *"thermochemical data of pure substances"*, VCH, Weinheim, 1993.
11 D. Rodney, and G. Martin, *Phys. Rev. B*, **61**, 8714 (2000).
12 Y. N. Osetsky, and D. J. Bacon, *Modelling Simul. Mater. Sci. Eng.*, **11**, 427 (2003).
13 M. S. Daw, S. M. Foiles, and M. I. Baskes, *Mater. Sci. Rep.*, **9**, 251(1993).
14 T. Rasmussen, K. W. Jacobsen, T. Leffers, and O. B. Pedersen, *Phys. Rev. B*, **56**, 2977(1997).
15 S. J. Plimpton, LAMMPS, Sandia National Laboratories, 2008: http://lammps.sandia.gov/.
16 J. A. Zimmerman, C. L. Kelchner, P. A. Klein, J. C. Hamilton, and S. M. Foiles, *Phys. Rev. Lett.*, **87**, 165507 (2001).
17 V. Vitek, *Cryst. latt. Defects*, **5**, 1(1974).